

Article

A Novel Method for Estimating the State of Health of Lithium-Ion Batteries Based on Physics-Informed Neural Network

Yuxuan Deng ^{1,2,3} , Changqing Du ^{1,2,3,*}  and Zhong Ren ⁴

¹ Hubei Key Laboratory of Advanced Technology for Automotive Components, Wuhan University of Technology, Wuhan 430070, China; 286287@whut.edu.cn

² Foshan Xianhu Laboratory of the Advanced Energy Science and Technology Guangdong Laboratory, Foshan 528200, China

³ National Energy Key Laboratory for New Hydrogen-Ammonia Energy Technologies, Foshan Xianhu Laboratory, Foshan 528200, China

⁴ Vehicle Measurement, Control and Safety Key Laboratory of Sichuan Province, Xihua University, Chengdu 100089, China; renzhong@xhu.edu.cn

* Correspondence: cq_du@whut.edu.cn

Abstract: An accurate state of health (SOH) assessment of lithium-ion batteries is essential for ensuring the reliability and safety of electric vehicles (EVs). Data-driven SOH estimation methods have shown promise but face challenges in generalizing across diverse battery types and variable operating conditions. To address this, this study integrates physical information into data-driven approaches, enabling physically consistent inferences and a rapid adaptation to different battery chemistries and usage scenarios. Specifically, physical features correlated with battery degradation, such as the link between incremental capacity (IC) peaks and SOH, are used as constraints to guide model learning. A fully connected layer within a back-propagation neural network (BPNN) is employed to capture battery aging dynamics effectively. Experimental results on two datasets show that the proposed model outperforms traditional neural networks, reducing the RMSE by at least 1.1% and demonstrating strong generalizability in both single-dataset and transfer learning tasks.



Academic Editor: Claudio Gerbaldi

Received: 22 December 2024

Revised: 17 January 2025

Accepted: 24 January 2025

Published: 26 January 2025

Citation: Deng, Y.; Du, C.; Ren, Z. A Novel Method for Estimating the State of Health of Lithium-Ion Batteries Based on Physics-Informed Neural Network. *Batteries* **2025**, *11*, 49.

<https://doi.org/10.3390/batteries11020049>

Copyright: © 2025 by the authors. Licensee MDPI, Basel, Switzerland. This article is an open access article distributed under the terms and conditions of the Creative Commons Attribution (CC BY) license (<https://creativecommons.org/licenses/by/4.0/>).

1. Introduction

With the rapid development of the electric vehicle (EV) industry, lithium-ion (Li-ion) batteries have become the primary energy source for EVs due to their high energy density, long lifespan, and efficient charging/discharging performance [1]. The technical advantages of Li-ion batteries have driven their increasing adoption in the EV market. However, as the usage and number of Li-ion batteries continue to rise, their performance inevitably degrades during prolonged cycling and storage, particularly under the complex and dynamic operational environments of EVs [2]. This degradation, often manifesting as capacity fading, can sometimes lead to safety incidents. While lithium-ion (Li-ion) batteries have indeed played a transformative role in modern life, their aging and health management have also become critical areas of concern [3]. To ensure the long-term, safe, and reliable operation of Li-ion batteries, battery management systems (BMSs) are implemented to monitor various battery states [4]. Among these, the state of health (SOH)

is a key factor in guaranteeing the safe operation of EVs. Accurately monitoring and predicting the SOH of batteries is, therefore, one of the core tasks of BMSs [5].

In order to address the challenges mentioned above, various SOH estimation methods have been proposed by the academic community over the past decades. However, due to the complex electrochemical properties and highly nonlinear behavior of lithium-ion batteries, as well as the diverse and dynamic operating conditions they face, accurately estimating and predicting the SOH of lithium batteries remains a significant challenge [6]. In general, current SOH estimation methods can be broadly categorized into model-based and data-driven approaches. Model-based methods develop high-fidelity models, either from mathematical or physical perspectives, to assess the battery performance and lifespan [7]. These methods can be classified into electrochemical models and equivalent circuit models based on the modeling mechanism. Electrochemical modeling approaches aim to describe the thermodynamics, lithium-ion diffusion processes, SEI film thickness, and side reaction kinetics inside the battery, striving for the most accurate battery modeling and state estimation [8].

For example, Gao et al. [9] used the Padé approximation to simplify the rigorous P2D electrochemical model and assess battery aging based on three key aging factors, lithium-ion loss, the loss of active material, and increased resistance, ultimately achieving better accuracy. The method based on equivalent circuit modeling uses circuit elements (resistors, capacitors, and voltage sources) to explain various battery phenomena. For instance, Xu et al. [10] employed an equivalent circuit model to represent the battery, applied the recursive least squares method for online parameter identification, and then used an unscented Kalman filter to estimate the battery state. The use of a filter-based approach is also a common step in equivalent-circuit-model-based methods. For example, Jiang et al. [11] proposed an improved EKF design for co-estimating the state of charge (SOC) and state of health (SOH). The proposed method combines innovative strategies to overcome covariance traps and objectively compute the optimal covariance matrix configuration, thereby improving the accuracy of the traditional EKF. Although model-based approaches can characterize certain battery mechanisms with high accuracy, the models they rely on require extensive dedicated experiments for calibration, which is resource-intensive [12]. Additionally, most physical models are subject to specific conditions, limiting their transferability and noise immunity. With the advancement in technology, data-driven methods have been widely applied in SOH estimation. These approaches treat batteries as a “black box” and utilize machine learning (ML) to extract features from extensive aging data for the health state evaluation. Since data-driven methods do not require complex battery modeling or an in-depth analysis of degradation mechanisms, they have become increasingly popular [13]. Commonly used methods include shallow neural networks, deep learning (DL), support vector machines (SVMs), Gaussian process regression (GPR), etc. Ren et al. [14] proposed a multi-feature extraction strategy combined with a particle swarm optimization–nonlinear autoregressive exogenous input neural network (PSO-NARXNN). The PSO algorithm was employed to optimize the hyperparameters of NARXNN, including input delay, feedback delay, and the number of hidden neurons, which enhanced the accuracy and robustness of the SOH estimation algorithm. He et al. [15] introduced an SOH estimation method based on Gaussian process regression (GPR). This method extracted coefficient of variation features from partial charging voltage and current profiles as health factors and incorporated an improved particle swarm optimization algorithm. The improvement involved a mutation factor and adaptive weight adjustment based on population diversity. The proposed SOH estimation framework was validated using the NASA battery dataset.

Despite the progress achieved by the aforementioned methods, SOH estimation still faces significant challenges in generalizability. Model-based methods rely on high-precision

battery models and require the extensive recalibration of numerous parameters when there are changes in battery materials or operating conditions [16]. These requirements limit their generalization capabilities. On the other hand, most data-driven methods, while capable of automatically learning from data, often disregard the aging mechanisms of lithium-ion batteries [17]. As a result, these methods may produce non-physical or impractical predictions when applied to unfamiliar datasets. Moreover, they require prolonged retraining for new operating conditions or datasets, and their accuracy is not guaranteed, further hindering their generalizability. To solve the above-mentioned problems, physics-informed neural networks (PINNs) integrate physical principles with data-driven approaches [18]. By leveraging physical knowledge to guide the learning process, PINNs can reduce the retraining time and ensure accuracy when dealing with unfamiliar datasets, thus significantly enhancing model generalizability [19]. For example, Wang et al. [20] extracted health factors solely from charging curves and utilized PINNs to model battery degradation attributes from the perspectives of empirical degradation and state-space equations. This approach successfully captured battery degradation dynamics and demonstrated high accuracy across three battery datasets. Similarly, Ye et al. [21] extracted features from the incremental capacity (IC) and differential temperature curves and incorporated the monotonic relationship between P-IC and SOH as physical constraints in the model's learning process, thereby improving the interpretability of the neural network predictions.

From the above discussion, it is evident that, although some explorations and innovations in PINNs have addressed certain issues in traditional SOH estimation, several challenges remain unresolved:

- Many existing PINN algorithms, such as those in [21,22], rely on a single source of health factors (HFs) and adopt conservative HF extraction strategies, resulting in limited data diversity and potentially affecting algorithm generalizability.
- While there are multiple approaches to integrating neural networks with physical information [23], selecting the most suitable method based on HF selection strategies, battery materials, operating conditions, and the desired accuracy of results remains an open problem.
- To assess the generalizability of PINNs, dedicated validation methods must be developed to rigorously test their performance.

In light of these challenges, this paper makes the following contributions:

- Two battery datasets with different materials and discharge conditions are selected, and a more comprehensive HF extraction strategy is implemented.
- To enhance generalizability, a conventional backpropagation neural network (BPNN) is augmented with a multilayer perceptron (MLP), which models battery degradation dynamics from the perspectives of empirical degradation and state-space equations. Monotonicity constraints are incorporated into the loss function, and both outputs collectively serve as inputs to the physical information component.
- A fine-tuned transfer-learning strategy is employed to evaluate the PINN's adaptability across the selected datasets, with the results compared against the BPNN and CNN for validation.

The remainder of the paper is organized as follows: Section 2 introduces the experimental datasets and feature extraction strategy and explains the used algorithms. Section 3 gives the results and discussions. Finally, the conclusions are summarized in Section 4. Its flowchart is shown in Figure 1. As shown in the figure, the experimental data obtained from the batteries are processed to extract and select health factors. These factors are first input into the BPNN to obtain the initial SOH. Subsequently, the initial SOH, health factors, and the partial derivatives of the initial SOH with respect to the health factors are fed

into the MLP to model the battery degradation dynamics. The overall loss function of the network comprises three components: the BPNN loss, the MLP loss, and the monotonicity loss of the health factors.

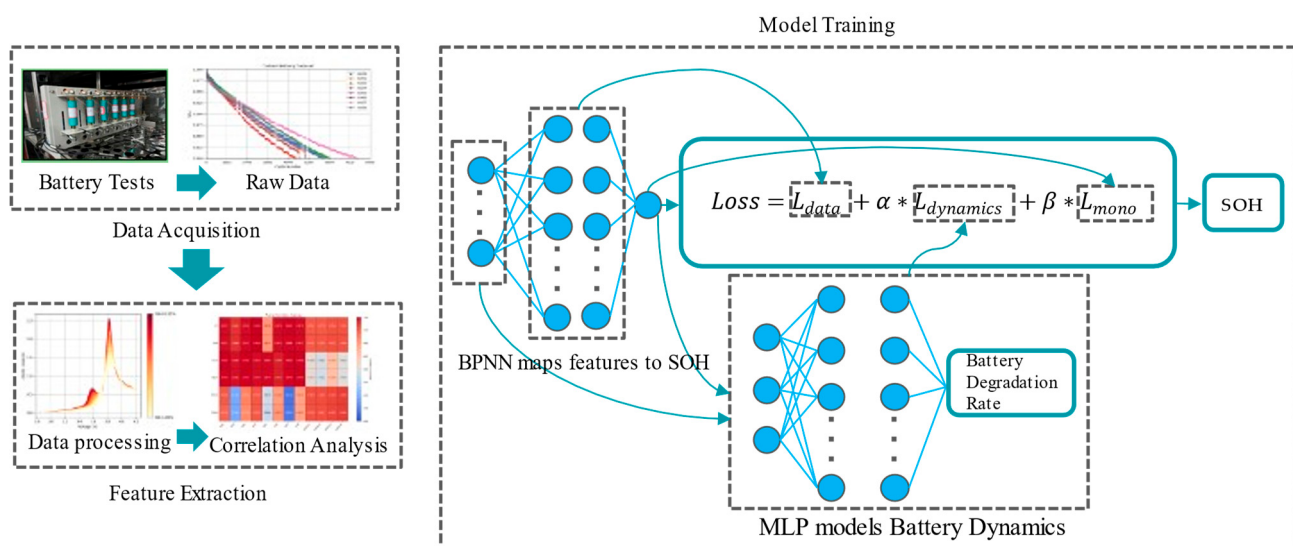


Figure 1. The flowchart of the PINN training scheme for battery state-of-health estimation, illustrating data preprocessing, feature extraction, model training, and evaluation steps. Feature extraction was performed using the XJTU and Oxford datasets, and the training and test sets were divided according to a 6:4 ratio. Both the BPNN and PINN models were trained based on this division ratio and further adjusted using the loss function shown in the figure.

2. Experimental Datasets

With reference to recent studies, this paper utilizes two open-source aging datasets provided by the University of Oxford [24] and Xi'an Jiaotong University (XJTU) [25], referred to as the Oxford dataset and the XJTU dataset, respectively. This study uses data from these datasets: batteries numbered 1 through 8 from the Oxford dataset, and batteries numbered 1 through 4 from batch 1 of the XJTU dataset. Details are provided below.

2.1. Oxford Aging Dataset

The Oxford aging dataset includes eight LiCoO₂ pouch batteries with a nominal capacity of 0.74 Ah. Aging experiments were conducted at 40 °C. The batteries were discharged using driving cycles derived from the Urban Artemis profile (average current = 1.36 A) until the terminal voltage reached 2.7 V. Subsequently, the batteries were subjected to constant-current (CC) charging at a 2C rate until the terminal voltage reached 4.2 V. This charge–discharge cycle was repeated 100 times, followed by characterization tests to measure battery capacity. Specifically, the charging protocol in the Oxford dataset employs constant-current charging (CC mode), while the discharging process is conducted under dynamic operating conditions based on the driving cycles derived from Artemis curves. The degradation trajectories of the eight batteries in this dataset are shown in Figure 2.

2.2. XJTU Aging Dataset

The dataset includes 55 lithium-ion batteries subjected to six different charging and discharging strategies, with their operation-to-failure data recorded. These strategies include fixed charging and discharging, random discharging with a fixed current in two different cycles, random walking, and the charging and discharging strategy of a satellite in geosynchronous Earth orbit (GEO). The experimental batteries are divided into six distinct batches based on these different strategies. The selected batteries were manufactured by Lixin and have a chemical composition of LiNi_{0.5}Co_{0.2}Mn_{0.2}O₂. They have a nominal

capacity of 2000 mAh, a nominal voltage of 3.6 V, a charging cutoff voltage of 4.2 V, and a discharge cutoff voltage of 2.5 V. For this study, four cells from the first batch were selected, with the operating conditions involving constant-current charging and constant-current discharging. The degradation trajectories of these four cells are shown in Figure 3.

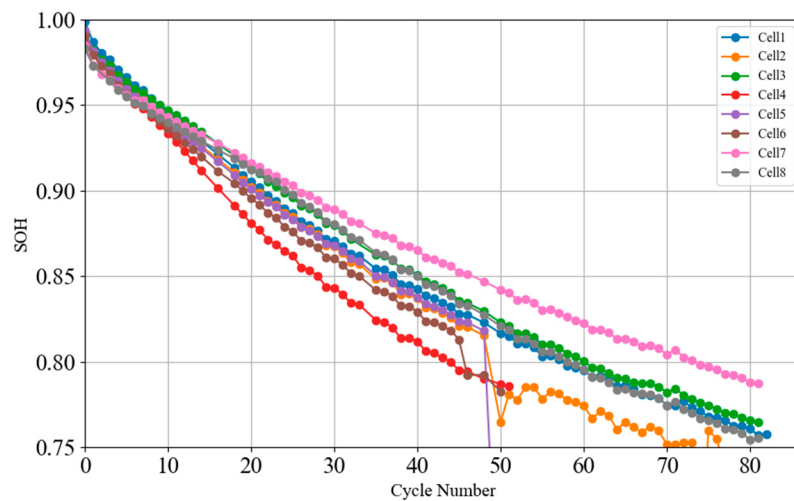


Figure 2. Oxford battery dataset capacity degradation. The aging experiment was conducted at 40 °C with constant-current charging (CC mode), and the discharging process was carried out under dynamic operating conditions. Further details are provided above.

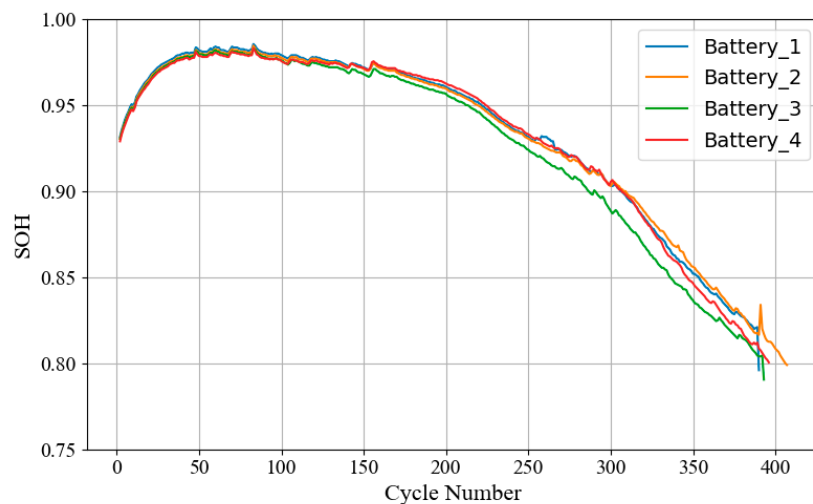


Figure 3. XJTU battery dataset capacity degradation. The aging experiment was at the room temperature with constant-current charging (CC mode), and the discharging process was constant-current discharging. Further details are provided above.

2.3. Aging Analysis and Feature Extraction

The aging of Li-ion batteries is typically characterized by capacity fade, increased internal resistance, and changes in the charge/discharge curve shapes. These degradation trends visually reflect the aging state of the battery. By extracting health factors (Health Factors, HF), these trends can be quantitatively assessed, thereby further evaluating the aging status of the battery. The selection strategy for health factors plays a crucial role in the performance of the final model. Therefore, when choosing health factors, it is important to follow principles such as easy accessibility, suitability for real-world operating conditions, and a high correlation with aging, while also considering their adaptability and generalizability across different battery types.

In line with this approach, we aim to minimize the input dimensionality of the neural network while ensuring model accuracy and robustness. To this end, this section employs a generalized health factor extraction strategy based on the analysis of two open-source battery aging datasets. In this strategy, we extract health factors from the charge curves, discharge curves, and incremental capacity (dQ/dV) curves in each dataset. These factors are then quantitatively analyzed for their correlation with battery aging, and the factor most strongly correlated with aging is selected as the input for the aging estimation model. This generalized strategy ensures the accuracy and robustness of the model while maintaining its applicability and generalizability across different battery types.

2.3.1. Charging Curve

From the charging process, the constant-current charging process takes less and less time under the same charging rate because the capacity of Li-ion batteries decreases with the aging of Li-ion batteries. From the charging voltage curve of Oxford Cell1, there is an inflection point at 3.8 V, and the change of charging voltage curve is more obvious in the range of 3.8 V to 4.2 V, as shown in Figure 4.

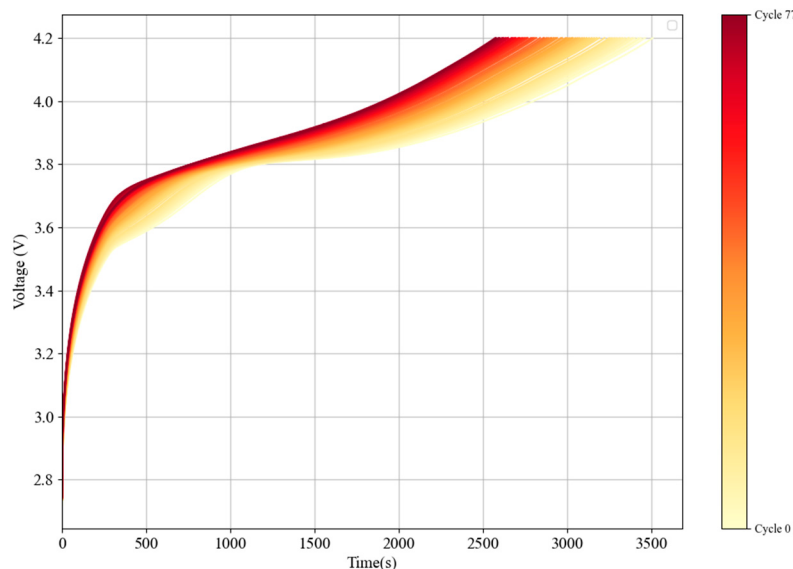


Figure 4. Charging curve of Oxford battery dataset, which was conducted at 40 °C with constant-current charging (CC mode).

For the XJTU dataset, the charging process includes a constant-voltage phase. To ensure consistency with the Oxford dataset, we focus on the constant-current charging portion. As seen in the curve of Battery 1 (Figure 5), there is a distinct inflection point around 3.8 V, after which the process transitions to constant-voltage charging at 4.2 V. Therefore, for both datasets, the Charged Time During Equal Voltage Increase (CTEVI) from 3.8 V to 4.1 V is selected as a health factor. Since the current magnitude remains constant during constant-current charging, once the time required for a given voltage increase is known, the corresponding charged capacity (Charged Capacity During Equal Voltage Increase, CCEVI) can be easily calculated as another health factor. It is important to note that, because the Oxford dataset does not include a constant-voltage phase, while the XJTU dataset does, health factors related to constant-voltage charging are not considered.

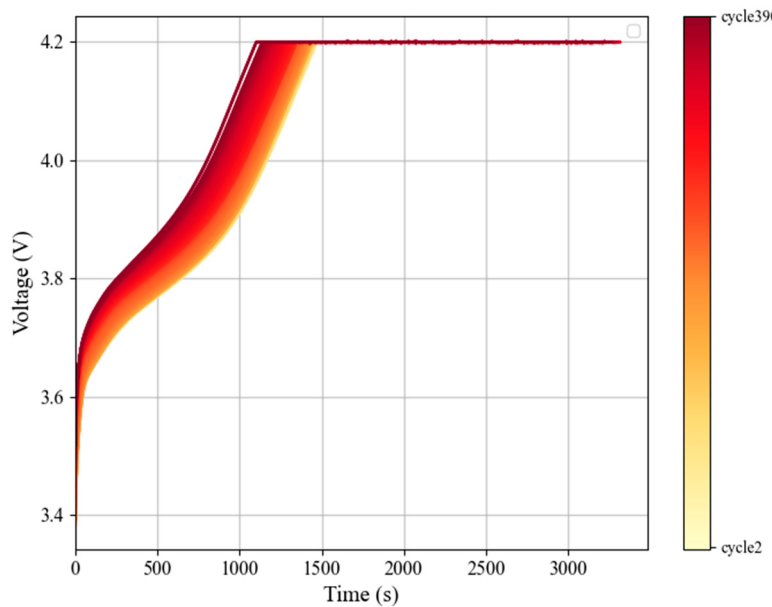


Figure 5. Charging curve of XJTU battery dataset, which was at the room temperature with constant-current charging (CC mode).

2.3.2. Discharge Curves

Although the batteries in the two datasets were tested under different operating conditions, their discharge curves exhibit certain similarities. Overall, as the batteries continue to age, the time required to discharge to the lower cutoff voltage becomes shorter, and the slope of the discharge voltage increases. For both batteries, there is little distinction in the discharge voltage curve between 4.2 V and 3.7 V. However, below 3.7 V, a noticeable difference appears, as shown in Figures 6 and 7. Therefore, the time from 3.7 V to the end of discharge (Discharged Time During Equal Voltage Decrease, DTEVD) and the capacity discharged during this time (Discharged Capacity During Equal Voltage Decrease, DCEVD) are selected as health factors.

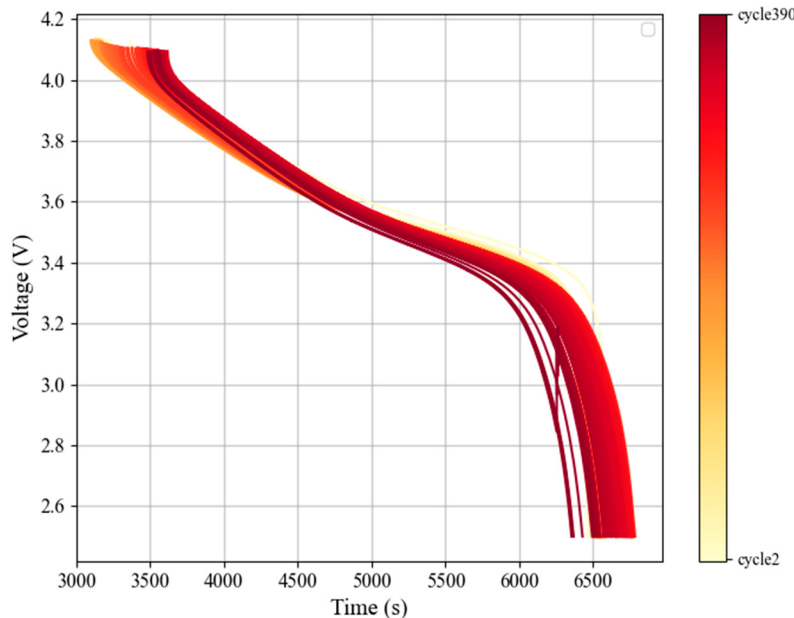


Figure 6. Discharging curve of XJTU battery dataset, which was carried out under constant current conditions.

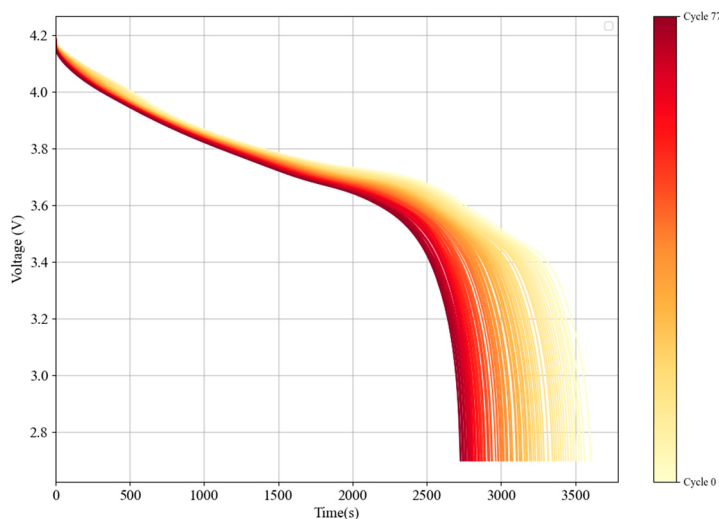


Figure 7. Discharging curve of Oxford battery dataset, which was carried out under dynamic operating conditions.

2.3.3. Incremental Capacity Curve

Incremental curve analysis (ICA) is a commonly used method to analyze the aging mechanism of LiB, which can transform the plateau curve of voltage into the informative IC curve; the wave peaks in the IC curves represent different phase transition processes during the charging and discharging phases of LIBs, and the information such as the height and position of the wave peaks can present certain information [26,27]. This information can effectively characterize the insertion and extraction process of lithium-ion active materials, thus revealing the phase transition properties within LIBs. Therefore, the IC curve analysis is considered a key technique to study the aging mechanism of LIBs.

The following differential equation can be used to calculate the IC curve from the CC charging process:

$$IC = \frac{dQ}{dV} = \frac{Q_{t+1} - Q_t}{V_{t+1} - V_t}, \quad (1)$$

where Q and V denote the capacitance and voltage, respectively. Q_t denotes the charging capacity at moment t , and V_t denotes the terminal voltage at the moment t , and t denotes the sampling time.

The original IC curve processed in this way may have problems such as having sharp points or insignificant wave peaks, and Gaussian filtering is needed on top of this in order to obtain a smooth IC curve quickly. As shown in Figure 8, Oxford's IC curve has two obvious peaks after processing, and the shape of the curve changes significantly with the decrease in SOH; the most obvious is that the two peaks become one and the height of the second peak decreases at a low SOH.

As shown in Figures 8 and 9, the IC curve of XJTU has only one obvious wave peak after processing, and the shape of the curve changes significantly as the cycle progresses, and the height of the wave peak decreases. To summarize, we can use the peak value of the cell peak (IC Peak, ICP) and the area of the voltage region where the peak is located (Area of IC Peak, ICPA), in which, for the Oxford dataset with two peaks, we choose the second peak with more obvious changes.

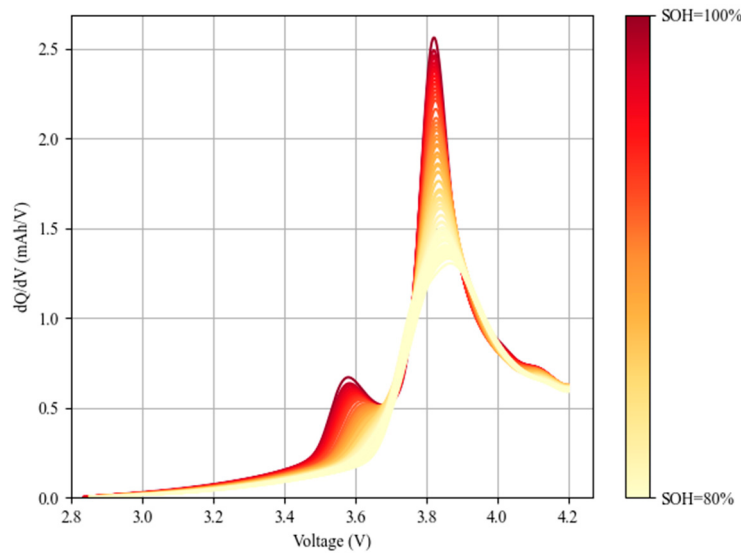


Figure 8. The IC curves of Oxford battery dataset.

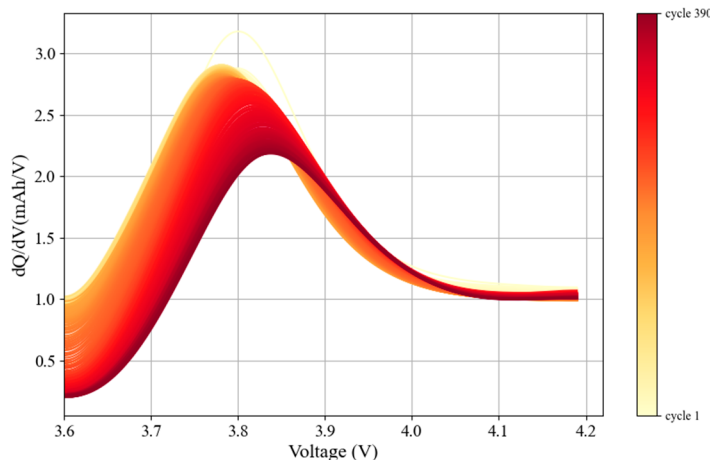


Figure 9. The IC curves of XJTU battery dataset.

2.3.4. Feature Extraction

The above discussion has analyzed and extracted the health factors from the two datasets, and these screened health factors were subjected to Pearson's correlation analysis, which is a valid method for assessing the degree of correlation between two continuous variables. The expression is given below:

$$\rho = \frac{\sum_{i=1}^n ((HF_i - \bar{HF})(SOH_i - \bar{SOH}))}{\sqrt{\sum_{i=1}^n (HF_i - \bar{HF})^2 \sum_{i=1}^n (SOH_i - \bar{SOH})^2}}, \quad (2)$$

where ρ is the Pearson correlation coefficient of \bar{HF} and \bar{SOH} denote the mean values of the health factor and SOH, respectively, and the results for both datasets are shown in Figure 10.

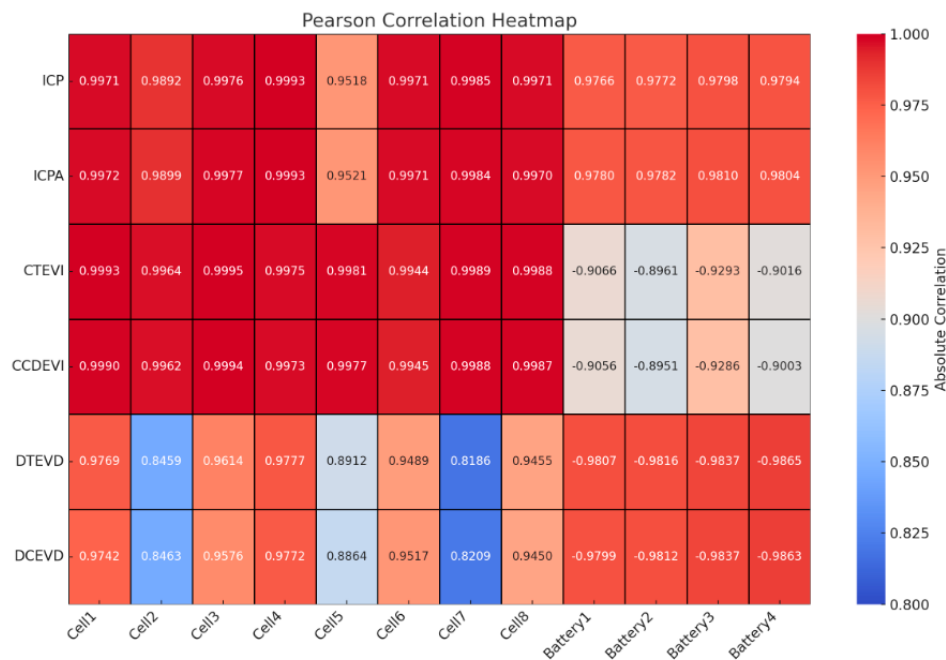


Figure 10. Heat map of the Pearson correlation coefficient of each battery.

It can be seen that the average values of the ICPA and ICA correlation coefficients of XJTU and Oxford are above 0.95, which can illustrate the monotonous limiting relationship of IC curves to SOH; moreover, the correlation coefficients of CTEVI and CCDEVI are above 0.9, indicating that the correlation coefficients selected before are all strongly correlated with SOH. Specifically, the correlation coefficients of ICPA in the selected samples range from a maximum value of 0.9993 to a minimum value of 0.9518, with an average value as 0.9867. The correlation coefficients of ICP in the selected samples range from a maximum value of 0.9993 to a minimum value of 0.9521, with an average value as 0.9872. The correlation coefficients of CTEVI in the selected samples range from a maximum value of 0.9995 to a minimum value of 0.8961, with an average value as 0.9681. The correlation coefficients of CCDEVI in the selected samples range from a maximum value of 0.9994 to a minimum value of 0.8951, with an average value as 0.9676. Therefore, the selected health factors are CTEVI, CCDEVI, ICP, and ICPA.

2.4. Network Structure

Considering the complexity of the reaction mechanisms in lithium-ion power batteries, and their strong nonlinearity and time-varying nature, as well as the need to perform nonlinear mapping for a large volume of input–output data, the Backpropagation Neural Network (BPNN) is an effective method for SOH estimation [28]. It continuously adjusts the network's weights and thresholds through backpropagation to minimize the sum of squared errors, thereby simulating the human brain's data processing capabilities [29]. The BPNN topology consists of an input layer, hidden layers, and an output layer, with the gradient descent method used to find the optimal solution. In this study, the BPNN structure includes six input dimensions, one output dimension, three layers, fifty hidden dimensions per layer, and a dropout rate of 0.008. These configurations were selected based on preliminary experiments to balance the trade-off between model complexity and prediction accuracy. For an r -dimensional input layer vector $X = (x_1, x_2, x_3 \dots x_r)^T$, s -dimensional hidden layer vector $H = (h_1, h_2, h_3 \dots h_s)^T$, and t -dimensional output layer vector $Y = (y_1, y_2, y_3 \dots y_t)^T$, the main steps of BPNN are as follows:

1. Calculate the expected output, the health factor, and time as input information entered into the input layer through forward propagation; the layers of the network are

calculated in a specified order, and the output layer receives the output results as shown in Equation (3) and (4):

$$h_j = f\left(\sum_{j=1}^r w_{ij}^1 x_j + b_j^1\right), \quad (3)$$

$$d_j = f\left(\sum_{j=1}^s w_{ij}^2 h_j + b_j^2\right), \quad (4)$$

where $w_{ij}^l, l = 1, 2$ is the weight between the i -th neuron in layer l and the j -th neuron in layer $l + 1$. $b_j^l, l = 1, 2$ is the bias of the j -th neuron in layer $l + 1$. $f(\cdot)$ is the activation function, and the sin function chosen in this paper.

2. The error calculation, usually the loss function of traditional neural networks, is defined as the mean square error:

$$L_{data} = \frac{1}{2N} \sum_{i=1}^N \sum_{j=1}^N (d_{ij} - y_{ij})^2, \quad (5)$$

where N denotes the number of training samples

3. Update the weights and biases:

$$w_{ij}^l = w_{ij}^l - \alpha \frac{\partial L}{\partial w_{ij}^l}, l = 1, 2, \quad (6)$$

$$b_j^l = b_j^l - \alpha \frac{\partial L}{\partial b_j^l}, l = 1, 2, \quad (7)$$

where α is the learning rate, and L is the value of the loss function.

The error is backpropagated through the network, continuously updating the weights and thresholds to optimize the network. The training process iterates until the error requirement is met or the maximum number of iterations is reached. From this, it can be seen that the advantage of BPNN lies in its ability to perform the nonlinear mapping of inputs and outputs for large datasets, with a certain degree of self-learning and adaptive capability, making it widely applicable in various scenarios. However, it also becomes apparent that the adaptive ability of BPNN is based on adjusting the network weights during training, relying solely on the loss function for a single dataset (L_{data}) without considering other factors. This may result in performance degradation when encountering unfamiliar datasets and may not guarantee an optimal performance after retraining. Therefore, from this perspective, the generalization ability of the BPNN needs to be improved.

To address the issues mentioned above, this paper optimizes the BPNN by incorporating additional considerations into the loss function. As shown in Figure 11, the health factors are first introduced into the BPNN. Subsequently, as described in [15], battery degradation dynamics are integrated during the training process. Specifically, the battery degradation rate can be represented by a multivariate function, but its explicit form is difficult to determine. Therefore, a multilayer perceptron (MLP) is used to approximate this multivariate function, taking the health factors, predicted SOH, and the first derivative of the health factor with respect to SOH as inputs to the MLP. The actual time derivative of the SOH is used as benchmark data, thereby constructing a multivariate function to model the battery aging process. The loss function calculation for this process is shown in Equation (8):

$$L_{dynamics} = \frac{1}{N} \sum_{i=1}^N (\hat{SOH}_t - SOH_t)^2 \quad (8)$$

In addition to this based on the previous analysis of the IC curve and the literature [21], the monotonic relationship between the peak of the IC curve and the SOH can

be incorporated into the neural network as physical information with the addition of a loss function:

$$L_{mono} = \frac{1}{N} \sum_{i=1}^N \text{ReLU} \left(\frac{\partial \hat{SOH}}{\partial X_{IC}} \right) \quad (9)$$

where $\frac{\partial \hat{SOH}}{\partial X_{IC}}$ represents the partial derivative of \hat{SOH} with respect to X_{IC} , and X_{IC} represents the feature values extracted from the Incremental Capacity (IC) section.

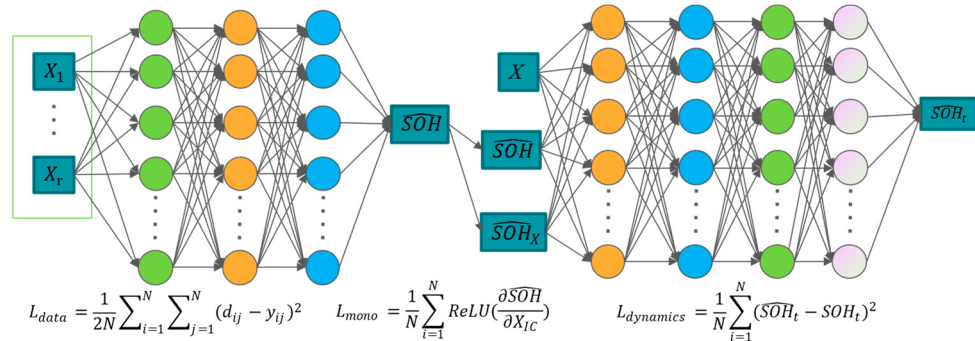


Figure 11. The layer configuration and learning mechanism of the PINN model.

The final loss function for the whole network is as follows:

$$\text{Loss} = L_{data} + \alpha * L_{dynamics} + \beta * L_{mono} \quad (10)$$

where α, β is the parameter. This gives the whole model the ability to adjust the network weights from the perspectives of two battery degradation mechanisms: the battery degradation kinetics and IC curve analysis.

After constructing the PINN, it is initially validated on each of the two selected datasets. To assess whether the generalization capability of the PINN has been improved, transfer learning experiments are then conducted. The evaluation approach involves selecting one of the aging datasets as the source domain and using the other dataset as the target domain. The base model is first trained using a randomly selected battery from the source domain. Subsequently, a battery from the target domain is randomly chosen, and the base model is fine-tuned using its cycle data. Finally, the re-trained model is tested using the remaining batteries from the target domain. The specific results are presented in detail in the next chapter. Notably, the average RMSE between the PINN predictions and the actual values is 0.0053, indicating that the overall RMSE is small and does not exhibit systematic patterns of bias. This suggests that the model does not have significant systematic biases. Overall, the PINN model maintains relatively low RMSE and MAPE values under all conditions, indicating good accuracy and stability across different scenarios. The low RMSE reflects the model's robustness against outliers, demonstrating its ability to handle noise or extreme data points while maintaining reliable performance. Meanwhile, the low MAPE signifies the model's high precision in terms of the overall prediction error, enabling the accurate estimation of the battery state of health across various battery types, operating conditions, and data distributions.

3. Results and Discussion

This section provides a detailed account of the results obtained using the proposed generic health factor extraction strategy and PINN for SOH estimation on a single aging dataset, with a comparison to BPNN and CNN. Additionally, the effectiveness of the proposed PINN algorithm under the fine-tuning-based transfer-learning strategy is verified

across different types of batteries, and the potential improvement relative to the BPNN is evaluated.

To assess the prediction accuracy, commonly used statistical metrics such as the Mean Absolute Percentage Error (MAPE) and Root Mean Square Error (RMSE) are employed for the quantitative evaluation. The MAPE measures the overall prediction error by calculating the percentage difference between each predicted value and the true value, then averaging it. In contrast, the RMSE is more sensitive to outliers and can be used to assess the robustness of the model.

$$MAPE = \frac{1}{N} \sum_{i=1}^N \left| \frac{\overline{SOH}_i - SOH_i}{SOH_i} \right|, \quad (11)$$

$$RMSE = \sqrt{\frac{1}{N} \sum_{i=1}^N (\overline{SOH}_i - SOH_i)^2}, \quad (12)$$

where \overline{SOH}_i denotes the estimated value of SOH, SOH_i denotes the true value of SOH, and N represents the number of samples.

3.1. Results on a Single Dataset

For each battery cycle data in the two datasets, XJTU and Oxford, the training and test sets were divided according to the ratio of 6:4, and both the BPNN and PINN were trained according to this division ratio, and the results are in Table 1.

Table 1. Estimation results of all cases in Oxford and XJTU dataset.

Dataset	Number	PINN		BPNN		CNN	
		RMSE	MAPE(%)	RMSE	MAPE(%)	RMSE	MAPE(%)
XJTU	1	0.0016	0.1434	0.0163	1.6795	0.0371	1.0151
	2	0.0033	0.2159	0.0153	1.7170	0.0477	1.5032
	3	0.0018	0.1688	0.1688	1.7133	0.0326	0.7715
	4	0.0027	0.2562	0.2562	2.3258	0.0463	1.2498
Oxford	1	0.0049	0.4915	0.0120	1.3209	0.0284	0.5337
	2	0.0120	0.9407	0.0288	3.3450	0.0530	3.7827
	3	0.0039	0.3892	0.0903	1.0085	0.0308	1.0970
	4	0.0022	0.2213	0.0068	0.7210	0.0249	0.7417
	5	0.0188	1.7164	0.0342	2.9132	0.0534	0.8023
	6	0.0050	0.5188	0.0092	0.8729	0.0303	0.6788
	7	0.0028	0.2403	0.0060	0.6252	0.0315	1.1602
	8	0.0047	0.4563	0.0157	1.7933	0.0380	1.4615

It can be observed that the average RMSE for the PINN on the XJTU dataset is 0.0024, with an average MAPE of 0.1961%, while the average RMSE for the BPNN on the XJTU dataset is 0.0188, with an average MAPE of 1.8589%. On the Oxford dataset, the average RMSE for the PINN is 0.0073, with an average MAPE of 0.6218%, while the average RMSE for the BPNN is 0.0153, with an average MAPE of 1.5750%. For the XJTU dataset, using the PINN instead of BPNN results in a reduction of approximately 87% in the RMSE and approximately 89% in the MAPE. On the Oxford dataset, the use of the PINN leads to a reduction of about 52% in the RMSE and about 60% in the MAPE compared to the BPNN. The specific prediction results can also be observed in the line charts. The line graph (Figures 12 and 13) shows the data for Cell 4 from the Oxford battery dataset. From the graph, it is evident that the PINN (BPNN-MLP) significantly improves the prediction accuracy compared to the BPNN.

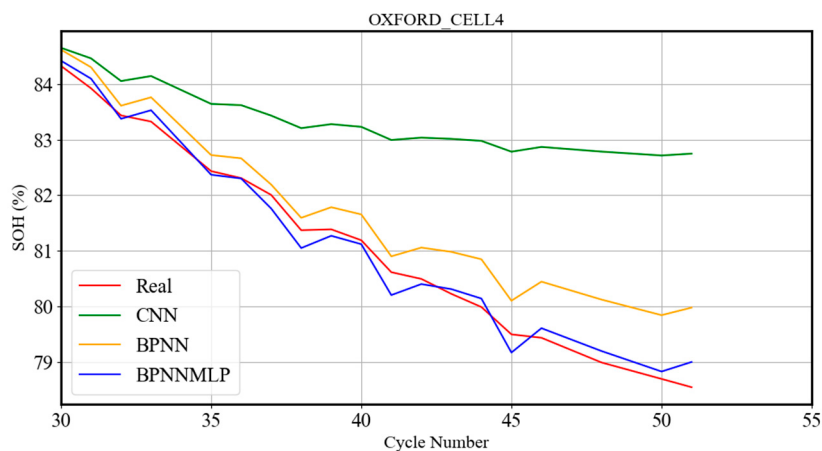


Figure 12. The performance of neural networks on the Oxford battery dataset.

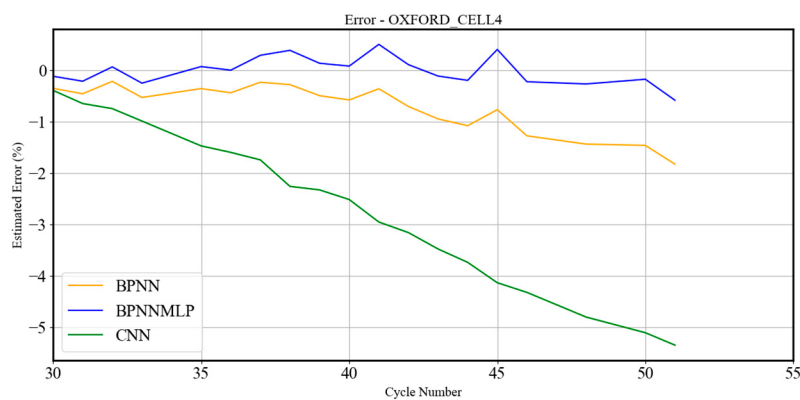


Figure 13. The error of neural networks on the Oxford battery dataset.

The line graph (Figures 14 and 15) shows the data for Battery 4 from the XJTU dataset. From the graph, it is evident that the PINN (BPNN-MLP) significantly improves the prediction accuracy compared to the BPNN. In terms of the relative error, the PINN consistently maintains an error below 0.5%, whereas the BPNN quickly reaches 3% in the later stages of cycling. Similarly, in the Oxford dataset, using Battery 4 as an example, the line graph shows that the PINN (BPNN-MLP) outperforms the BPNN in prediction accuracy. The PINN's relative error remains below 0.5%, while the BPNN's error increases to 1.5% in the later stages of the cycle.

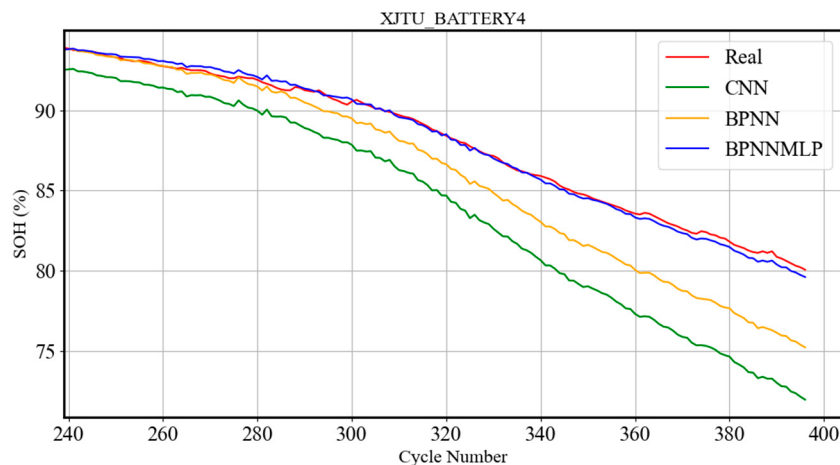


Figure 14. The performance of neural networks on the XJTU battery dataset.

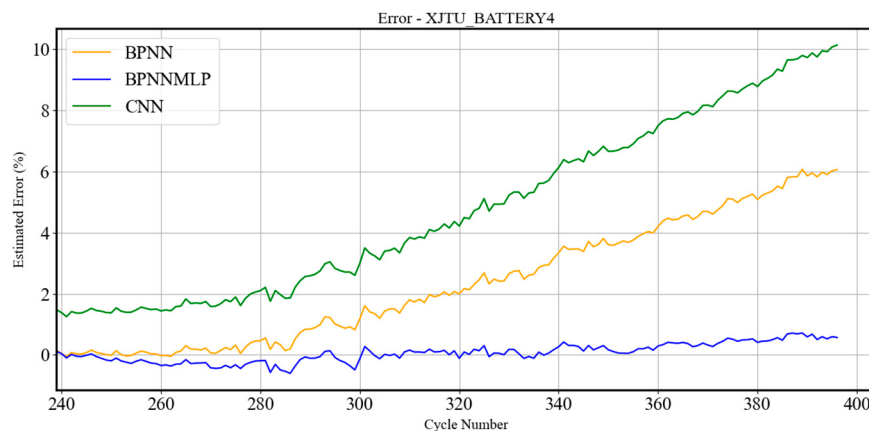


Figure 15. The error of neural networks on the XJTU battery dataset.

Based on these results, we can conclude that the PINN achieves a higher accuracy than the BPNN for the same dataset, and consistently produces better prediction results for each battery's cycling data.

3.2. Transfer Learning Validation

To verify the generalization and interpretability of the proposed PINN algorithm, validation experiments were conducted using transfer learning. The source and target domains were first determined. The PINN model was trained using cycling data from randomly selected batteries in the source domain. Two strategies, namely, model parameter fine-tuning and domain adaptation, are commonly employed in recent works for SOH estimation [30]. Among these, parameter fine-tuning is a more straightforward and efficient approach. Moreover, the primary differences between the two selected datasets lie in the experimental temperature and discharging conditions, which may affect the model's ability to adapt to the target data, particularly when the temperature and discharging conditions significantly influence the battery performance. To mitigate these effects, we selected the fine-tuning strategy, adjusting certain model parameters to improve its performance on the target domain. A fine-tuning transfer-learning strategy was then applied, where a battery from the target domain was randomly selected, and its cycling data were used to fine-tune the base model. During fine-tuning, only the final connection layer was updated, while the other layers were frozen. Finally, the retrained model was evaluated using other batteries from the target domain.

When the XJTU dataset is selected as the source domain and the Oxford dataset as the target domain, the results are presented in Table 2. In this case, Battery 4 from the Oxford dataset was used for fine-tuning. The results indicate that PINN transfer learning achieved an average RMSE of 0.01 and an average MAPE of 0.868%, while the BPNN yielded an average RMSE of 0.023 and an average MAPE of 2.229%. This represents a reduction in RMSE by 56.27% and MAPE by 61.07% for the PINN compared to the BPNN, demonstrating a significant improvement in prediction accuracy across all battery cycles.

Similarly, when Oxford is chosen as the source domain and XJTU as the target domain, the results are shown in Table 3. In this case, Battery 4 from the XJTU dataset was used for fine-tuning. The results show that PINN transfer learning achieved an average RMSE of 0.011 and an average MAPE of 1.16%, whereas BPNN produced an average RMSE of 0.019 and an average MAPE of 1.94%. This indicates a reduction in RMSE by 40.5% and MAPE by 39.9% for the PINN compared to the BPNN.

Table 2. The fine-tuning results when XJTU dataset is selected as the source domain.

Train	Test	PINN		BPNN		CNN	
		RMSE	MAPE(%)	RMSE	MAPE(%)	RMSE	MAPE(%)
XJTU Cell1	Oxford Cell2	0.020	1.922	0.036	4.093	0.250	4.383
	Oxford Cell3	0.003	0.278	0.014	1.685	0.006	0.366
	Oxford Cell4	0.006	0.620	0.022	2.620	0.021	2.668
	Oxford Cell5	0.027	1.601	0.047	2.139	0.047	0.074
	Oxford Cell6	0.005	0.600	0.018	1.984	0.013	1.111
	Oxford Cell7	0.004	0.348	0.011	1.261	0.012	2.186
	Oxford Cell8	0.007	0.706	0.015	1.822	0.016	2.883

Table 3. The fine-tuning results when Oxford dataset is selected as the source domain.

Train	Test	PINN		BPNN		CNN	
		RMSE	MAPE(%)	RMSE	MAPE(%)	RMSE	MAPE(%)
Oxford Cell1	XJTU Cell2	0.007	0.682	0.012	1.084	0.0123	1.5668
	XJTU Cell3	0.021	2.397	0.031	3.536	0.0220	3.2357
	XJTU Cell4	0.005	0.413	0.011	1.199	0.0234	0.1968

These results demonstrate that, under the selected transfer-learning strategy, the PINN provides a substantial improvement in accuracy over the BPNN, addressing the BPNN's generalization limitations and enhancing its performance.

3.3. Future Work

In this study, the effectiveness of the proposed PINN model for SOH estimation, using a generalized high-frequency feature extraction strategy and a fine-tuning-based transfer-learning strategy, was comprehensively validated using two open-source aging datasets with different material types and working conditions. However, several limitations remain. First, LiFePO4 (LFP) cells were not considered in this study. Second, the proposed PINN framework models battery degradation dynamics from the perspective of empirical degradation laws and state-space equations. With the availability of more data and internal variables, more sophisticated electrochemical models could be incorporated to capture battery aging dynamics. Finally, due to the small sample size of the Oxford dataset, the performance of the PINN on this dataset was lower compared to the XJTU dataset, and further exploration is needed in order to understand the underlying reasons for this performance difference across more datasets. In future research, we plan to explore a broader range of battery types and enhance the accuracy and generalization of the proposed method, tailoring it to the specific characteristics of different battery types. To address the aforementioned limitations, future work will focus on increasing the diversity of datasets and improving the model structure. By optimizing the model architecture, the proposed framework can better leverage diverse datasets, enabling it to perform more effectively on more datasets. Additionally, with the increased diversity of datasets, improvements in training methods will enhance the model's ability to learn from multi-source heterogeneous data.

4. Conclusions

A novel PINN framework is proposed for SOH estimation, evaluated on two datasets with different discharge conditions and battery materials. The methodology includes generalized feature extraction from charging curves, discharge curves, and incremental capacity curves, followed by a correlation analysis to identify relevant health factors.

Battery degradation dynamics are modeled using a multilayer perceptron (MLP) informed by empirical degradation laws and state-space equations. To ensure the physical consistency of SOH predictions, a monotonicity loss is incorporated into the loss function based on the monotonic relationship between incremental capacity parameters and SOH. Validation experiments, including individual and cross-dataset evaluations, are conducted using a fine-tuning-based transfer-learning strategy. The results demonstrate that the proposed framework achieves an RMSE and MAPE of less than 0.73% and 0.6218%, respectively, representing an improvement of at least 40% over baseline methods. These findings underscore the effectiveness, scalability, and generalization capabilities of the proposed PINN for the accurate SOH estimation in diverse battery systems.

Author Contributions: Conceptualization, Y.D. and C.D.; funding acquisition, C.D. and Z.R.; methodology, Y.D.; software, Pycharm 2023, Y.D.; supervision, C.D. and Z.R.; validation, Y.D.; visualization, Y.D.; writing—original draft, Y.D.; writing—review and editing, Z.R. and C.D. All authors have read and agreed to the published version of the manuscript.

Funding: This research was funded by the Key R&D project of Guangxi Province, China (AA23062058); and the Foshan Xianhu Laboratory of the Advanced Energy Science and Technology Guangdong Laboratory (XHRD2024-11233100-01).

Data Availability Statement: The two open-source aging datasets are available on the following websites: <https://ora.ox.ac.uk/objects/uuid:03ba4b01-cfed-46d3-9b1a-7d4a7bdf6fac> (accessed on 22 October 2023); and <https://doi.org/10.5281/zenodo.1096339> (accessed on 12 April 2024).

Conflicts of Interest: The authors declare that the research was conducted in the absence of any commercial or financial relationships that could be construed as a potential conflict of interest.

References

- Miao, Y.; Hynan, P.; von Jouanne, A.; Yokochi, A. Current Li-Ion Battery Technologies in Electric Vehicles and Opportunities for Advancements. *Energies* **2019**, *12*, 1074. [[CrossRef](#)]
- Rahman, T.; Alharbi, T. Exploring Lithium-Ion Battery Degradation: A Concise Review of Critical Factors, Impacts, Data-Driven Degradation Estimation Techniques, and Sustainable Directions for Energy Storage Systems. *Batteries* **2024**, *10*, 220. [[CrossRef](#)]
- Omariba, Z.B.; Zhang, L.; Sun, D. Review on Health Management System for Lithium-Ion Batteries of Electric Vehicles. *Electronics* **2018**, *7*, 72. [[CrossRef](#)]
- Sadegh Kouhestani, H.; Yi, X. Prognosis and Health Management (PHM) of Solid-State Batteries: Perspectives, Challenges, and Opportunities. *Energies* **2022**, *15*, 6599. [[CrossRef](#)]
- Dini, P.; Colicelli, A.; Saponara, S. Review on Modeling and SOC/SOH Estimation of Batteries for Automotive Applications. *Batteries* **2024**, *10*, 34. [[CrossRef](#)]
- Cui, X.; Hu, T. State of Health Diagnosis and Remaining Useful Life Prediction for Lithium-Ion Battery Based on Data Model Fusion Method. *IEEE Access* **2020**, *8*, 207298–207307. [[CrossRef](#)]
- Ren, Z.; Du, C. A Review of Machine Learning State-of-Charge and State-of-Health Estimation Algorithms for Lithium-Ion Batteries. *Energy Rep.* **2023**, *9*, 2993–3021. [[CrossRef](#)]
- Alkhedher, M.; Al Tahhan, A.B. Electrochemical and Thermal Modeling of Lithium-Ion Batteries: A Review of Coupled Approaches for Improved Thermal Performance and Safety Lithium-Ion Batteries. *J. Energy Storage* **2024**, *86*, 111172. [[CrossRef](#)]
- Gao, Y.; Liu, K.; Zhu, C.; Zhang, X.; Zhang, D. Co-Estimation of State-of-Charge and State-of-Health for Lithium-Ion Batteries Using an Enhanced Electrochemical Model. *IEEE Trans. Ind. Electron.* **2021**, *69*, 2684–2696. [[CrossRef](#)]
- Xu, Z.; Wang, J.; Lund, P.D.; Zhang, Y. Co-Estimating the State of Charge and Health of Lithium Batteries through Combining a Minimalist Electrochemical Model and an Equivalent Circuit Model. *Energy* **2022**, *240*, 122815. [[CrossRef](#)]
- Jiang, S.; Shi, J.; Borah, M.; Moura, S. Weaknesses and Improvements of the Extended Kalman Filter for Battery State-of-Charge and State-of-Health Estimation. In Proceedings of the 2024 American Control Conference (ACC), Toronto, ON, Canada, 8–12 July 2024; pp. 1441–1448.
- Khaleghi, S.; Hosen, M.S. Towards Machine-Learning Driven Prognostics and Health Management of Li-Ion Batteries. A Comprehensive Review. *Renew. Sustain. Energy Rev.* **2024**, *192*, 114224. [[CrossRef](#)]
- Guo, W.; Sun, Z.; Vilnsen, S.B.; Meng, J.; Stroe, D.I. Review of “Grey Box” Lifetime Modeling for Lithium-Ion Battery: Combining Physics and Data-Driven Methods. *J. Energy Storage* **2022**, *56*, 105992. [[CrossRef](#)]

14. Ren, Z.; Du, C.; Ren, W. State of Health Estimation of Lithium-Ion Batteries Using a Multi-Feature-Extraction Strategy and PSO-NARXNN. *Batteries* **2022**, *9*, 7. [[CrossRef](#)]
15. He, Y.; Bai, W.; Wang, L.; Wu, H.; Ding, M. SOH Estimation for Lithium-Ion Batteries: An Improved GPR Optimization Method Based on the Developed Feature Extraction. *J. Energy Storage* **2024**, *83*, 110678. [[CrossRef](#)]
16. Yang, K.; Zhang, L.; Zhang, Z.; Yu, H.; Wang, W.; Ouyang, M.; Zhang, C.; Sun, Q.; Yan, X.; Yang, S.; et al. Battery State of Health Estimate Strategies: From Data Analysis to End-Cloud Collaborative Framework. *Batteries* **2023**, *9*, 351. [[CrossRef](#)]
17. Reza, M.S.; Mannan, M. Recent Advancement of Remaining Useful Life Prediction of Lithium-Ion Battery in Electric Vehicle Applications: A Review of Modelling Mechanisms, Network Configurations, Factors, and Outstanding Issues. *Energy Rep.* **2024**, *11*, 4824–4848. [[CrossRef](#)]
18. Li, H.; Zhang, Z.; Li, T.; Si, X. A Review on Physics-Informed Data-Driven Remaining Useful Life Prediction: Challenges and Opportunities. *Mech. Syst. Signal Process.* **2024**, *209*, 111120. [[CrossRef](#)]
19. Fernández de la Mata, F.; Gijón, A.; Molina-Solana, M.; Gómez-Romero, J. Physics-Informed Neural Networks for Data-Driven Simulation: Advantages, Limitations, and Opportunities. *Phys. Stat. Mech. Its Appl.* **2023**, *610*, 128415. [[CrossRef](#)]
20. Wang, F.; Zhai, Z.; Zhao, Z.; Di, Y.; Chen, X. Physics-Informed Neural Network for Lithium-Ion Battery Degradation Stable Modeling and Prognosis. *Nat. Commun.* **2024**, *15*, 4332. [[CrossRef](#)]
21. Ye, J.; Xie, Q.; Lin, M.; Wu, J. A Method for Estimating the State of Health of Lithium-Ion Batteries Based on Physics-Informed Neural Network. *Energy* **2024**, *294*, 130828. [[CrossRef](#)]
22. Saleh, M.A.; Alquennah, A.N.; Ghrayeb, A.; Refaat, S.S.; Abu-Rub, H.; Khatri, S.P. A Self-Adaptive Physics-Informed Gated Recurrent Unit Neural Networks Model for Estimating the Lifetime of Li-Ion Batteries. *techRxiv* **2024**.
23. Wen, P.; Ye, Z.-S.; Li, Y.; Chen, S.; Xie, P.; Zhao, S. Physics-Informed Neural Networks for Prognostics and Health Management of Lithium-Ion Batteries. *IEEE Trans. Intell. Veh.* **2024**, *9*, 2276–2289. [[CrossRef](#)]
24. Christoph, R.B. *Diagnosis and Prognosis of Degradation in Lithium-Ion Batteries*; Department of Engineering Science University of Oxford: Oxford, UK, 2017.
25. Birk, C. Project-Physics-Informed Neural Network for Lithium-Ion Battery Degradation Stable Modeling and Prognosis. Ph.D. Thesis, University of Oxford, Oxford, UK, 2017.
26. Zhang, Q.; Li, X.; Zhou, C.; Zou, Y.; Du, Z.; Sun, M.; Ouyang, Y.; Yang, D.; Liao, Q. State-of-Health Estimation of Batteries in an Energy Storage System Based on the Actual Operating Parameters. *J. Power Sources* **2021**, *506*, 230162. [[CrossRef](#)]
27. Weng, C.; Feng, X.; Sun, J.; Peng, H. State-of-Health Monitoring of Lithium-Ion Battery Modules and Packs via Incremental Capacity Peak Tracking. *Appl. Energy* **2016**, *180*, 360–368. [[CrossRef](#)]
28. Waseem, M.; Huang, J. Data-Driven GWO-BRNN-Based SOH Estimation of Lithium-Ion Batteries in EVs for Their Prognostics and Health Management. *Mathematics* **2023**, *11*, 4263. [[CrossRef](#)]
29. Cheng, M.; Jiao, J. SOH Estimation of Lithium Batteries Based on New Health Factors and Optimized BP Neural Networks. In Proceedings of the 2023 19th International Conference on Natural Computation, Fuzzy Systems and Knowledge Discovery (ICNC-FSKD), Harbin, China, 29–31 July 2023; pp. 1–7.
30. Liu, K.; Peng, Q.; Che, Y.; Zheng, Y.; Li, K.; Teodorescu, R.; Widanage, D.; Barai, A. Transfer Learning for Battery Smarter State Estimation and Ageing Prognostics: Recent Progress, Challenges, and Prospects. *Adv. Appl. Energy* **2023**, *9*, 100117. [[CrossRef](#)]

Disclaimer/Publisher’s Note: The statements, opinions and data contained in all publications are solely those of the individual author(s) and contributor(s) and not of MDPI and/or the editor(s). MDPI and/or the editor(s) disclaim responsibility for any injury to people or property resulting from any ideas, methods, instructions or products referred to in the content.